ARTICLE OPEN

Check for updates

All-natural phyllosilicate-polysaccharide triboelectric sensor for machine learning-assisted human motion prediction

Yuanhao Liu[1,2], Yiwen Shen[1], Wei Ding[2], Xiangkun Zhang[1], Weiliang Tian[1]✉, Song Yang[3]✉, Bin Hui[2] and Kewei Zhang[1,2]✉

The rapid development of smart and carbon-neutral cities motivates the potential of natural materials for triboelectric electronics. However, the relatively deficient charge density makes it challenging to achieve high Maxwell's displacement current. Here, we propose a methodology for improving the triboelectricity of marine polysaccharide by incorporating charged phyllosilicate nanosheets. As a proof-of-concept, a flexible, flame-retardant, and eco-friendly triboelectric sensor is developed based on all-natural composite paper from alginate fibers and vermiculite nanosheets. The interlaced fibers and nanosheets not only enable superior electrical output but also give rise to wear resistance and mechanical stability. The fabricated triboelectric sensor successfully monitors slight motion signals from various joints of human body. Moreover, an effective machine-learning model is developed for human motion identification and prediction with accuracy of 96.2% and 99.8%, respectively. This work offers a promising strategy for improving the triboelectricity of organo-substrates and enables implementation of self-powered and intelligent platform for emerging applications.

npj Flexible Electronics (2023)7:21 ; https://doi.org/10.1038/s41528-023-00254-3

INTRODUCTION

As an emerging renewable energy technology, triboelectric nanogenerator based on the contact-electrification and electrostatic induction can convert ubiquitous mechanical energy from natural environment into electrical energy[1–5], providing an innovative solution for sustainable human development. According to the principle of triboelectric energy generation, self-powered wearable sensors without external power sources are widely studied and show great potential for monitoring human motions[6–10]. To acquire desirable performance, abundant studies have focused on optimizing favorable systems and circuits, while relatively less studies on engineering triboelectric materials[11–13]. Although almost all substances can essentially generate triboelectricity, it is essential to develop triboelectric materials with high charge densities in light of fundamental physical model of Maxwell's displacement current.

Natural polymer materials, featuring merits of eco-friendliness, low weight, superior flexibility, and machinability, offering significant advantage to prepare biocompatible devices for some special application purposes[14–16]. For example, fibrous cellulose papers possess microstructure without complementary surface roughening, accelerating their widespread application in bionic skin, implantable medical sensors and human-machine interaction[17–19]. Renewable, flame-retardant and biodegradable alginate fibers derived from marine algae are up-and-coming candidates for future flexible and wearable electronics[20–23]. However, the relatively deficient charge density makes it difficult to achieve high triboelectric output. In recent years, a steady stream of studies reported the modification of triboelectric materials by incorporating two-dimensional (2D) laminates, such as graphene[24], MXene ($Ti_3C_2T_x$)[8,25], molybdenum disulfide (MoS_2)[26], and hexagonal boron nitride (h-BN)[27]. The incorporated laminates can not only increase specific surface areas but also suppress the loss of as-generated triboelectric electrons, dramatically enhancing the triboelectric output. As a natural phyllosilicate mineral constructed by an octahedral layer of MgO and Fe_2O_3 sandwiched between two identical tetrahedral layers of SiO_2 and Al_2O_3[28,29], negatively charged vermiculite (VMT) lamellas has distinct advantages such as low cost, facile fabrication, surface charge behavior, and good stability against harsh conditions. It is thus expected to achieve comprehensive triboelectricity, flame-retardancy, and biodegradability by synergizing VMT lamellas with alginate fibers.

In this work, we proposed a methodology for improving triboelectric performance of marine polysaccharide-derived biofibers by incorporating natural VMT nanosheets. The composite paper was used as a desirable negative triboelectric material to construct a flexible, eco-friendly, flame-retardant, and biodegradable triboelectric nanogenerator. The interlaced alginate fibers and VMT nanosheets not only give the device superior electrical output performance, but also provide a tremendous improvement in flame retardance and mechanical stability. In particular, the fabricated triboelectric sensor successfully monitors slight motion signals from human body, making it a promising candidate for practical application in self-powered human healthcare and rehabilitation exercise. To attain the capability of selective identification for specific joint motions, an effective machine-learning (ML) model with extraordinary prediction accuracy and readability was developed by utilizing the feature data from principal component analysis (PCA).

RESULTS AND DISCUSSION

Exfoliation of phyllosilicate nanosheets

As shown in Fig. 1a, the expanded VMT is a layered material that consists of accordion-like pieces. As can be seen from the

[1]Key Laboratory of Chemical Engineering in South Xinjiang, College of Chemistry and Chemical Engineering, Tarim University, 843300 Alar, P. R. China. [2]State Key Laboratory of Bio-Fibers and Eco-Textiles, Collaborative Innovation Center for Marine Biomass Fibers, Materials and Textiles of Shandong Province, College of Materials Science and Engineering, Institute of Marine Biobased Materials, Qingdao University, 266071 Qingdao, P. R. China. [3]Department of Hepatology, Beijing Ditan Hospital of Capital Medical University, 100015 Beijing, P. R. China. ✉email: tianweiliang@taru.edu.cn; sduyangsong@163.com; zhkw@qdu.edu.cn

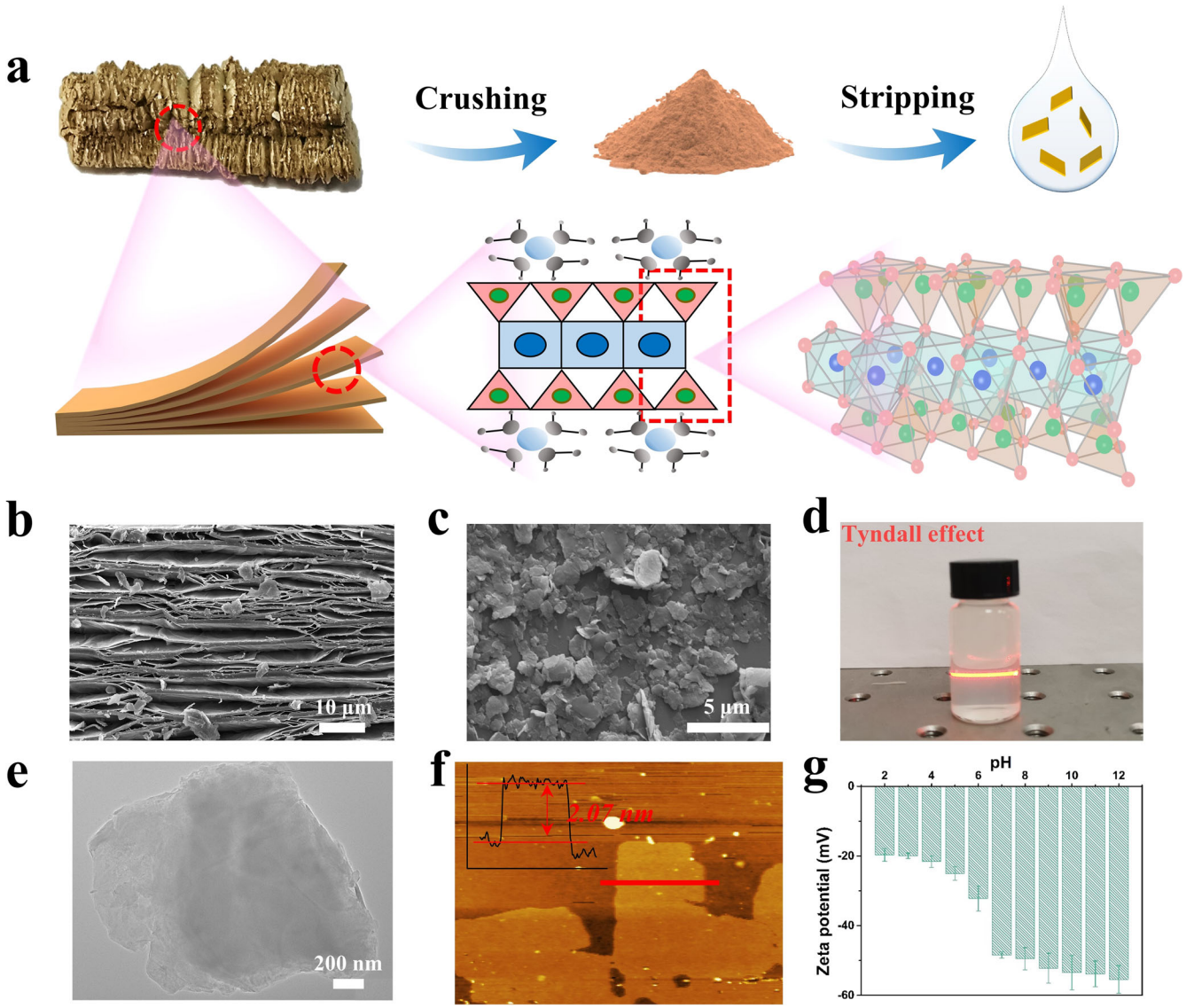

Fig. 1 Exfoliation of phyllosilicate nanosheets. a Schematic diagram of the exfoliation process of VMT nanosheets from expanded VMT with accordion-like morphology and the corresponding crystal structure of VMT. **b** SEM image of the expanded VMT crystal. **c** SEM image of the exfoliated VMT nanosheets. **d** Photograph of the VMT nanosheet solution, showing Tindal effect. **e** TEM image of the exfoliated VMT nanosheets. **f** AFM image and the corresponding height profile of the exfoliated VMT nanosheets. **g** Zeta potentials of the VMT dispersions at different pH values.

microscopic magnification schematic, the basic structure of the VMT nanosheet is mainly composed of two layers of silicate tetrahedra sandwiched by a layer of magnesium octahedra, forming sandwich structure. The cations in the hydrated layer are usually Mg^{2+} or Ca^{2+} [29,30]. Usually, some trivalent Al^{3+} will partially replace the central tetravalent Si^{4+} of the tetrahedral silicate in the sandwich structure, thus causing certain negative charge of the VMT nanosheets. The SEM (Fig. 1b) analysis indicates that the expanded VMT possesses a multilayer structure with varied layer spacing from macroscales to nanoscales, maybe owing to impurities and different interlayer cations. In order to obtain VMT nanosheets quickly and easily, we first grind the VMT particles into powder, and then directly add the VMT powder to an appropriate amount of deionized water in a cell crusher for ultrasonic stripping (Fig. 1a). This method saved a tedious process and a lot of time compared to the VMT nanosheets obtained by previous exfoliation using a two-step ion exchange method[31]. As can be seen from the SEM (Fig. 1c), the exfoliation yielded single or several layers of VMT nanosheets with lateral dimensions ranging from a few microns to tens of microns. The obtained colloidal suspension of VMT nanosheets displays a light brown color and can produce a significant Tyndall effect, as shown in Fig. 1d. The morphology and size of the monolayer VMT nanosheets are further clearly seen in TEM (Fig. 1e). To determine the thickness of the obtained nanosheets, a suspension of VMT nanosheets was spin-coated on silica and then characterized by atomic force microscopy (AFM), as shown in Fig. 1f. It is clear that the VMT nanosheets have a homogeneous thickness in the range of 1–3 nm, which facilitates stacking with the alginate fibers and attachment in the fiber voids to form a composite paper. As shown in Fig. 1g, the zeta potential of the obtained VMT nanosheet is about −50 mV, confirming the negatively charged nature of the VMT solution, and the solution keeps negatively charged in a wide pH range from 2 to 12.

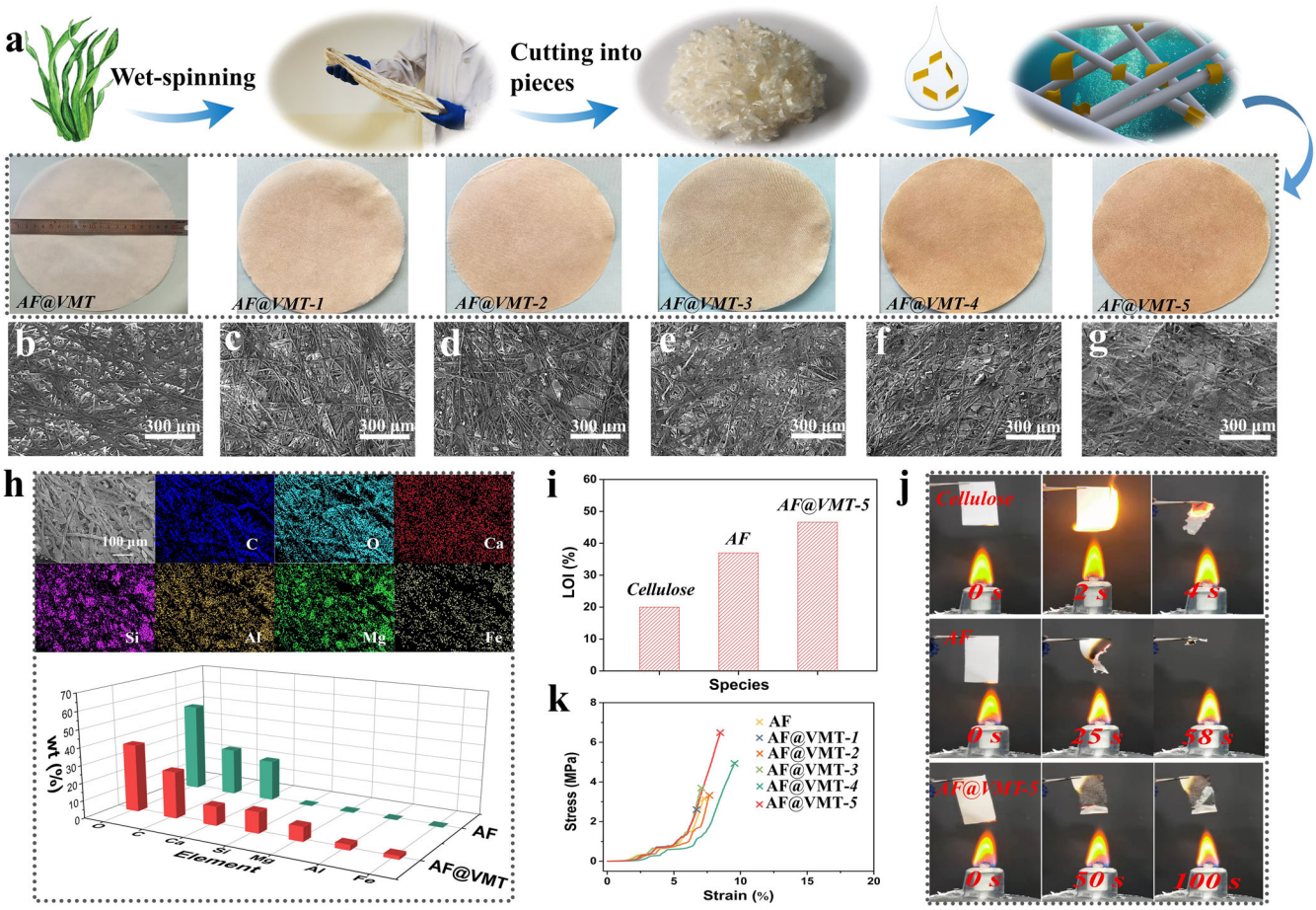

Fig. 2 Characteristics of all-natural composite paper. a Schematic diagram of the manufacture of the AF@VMT-x paper. **b**–**g** SEM images of (**b**) AF, (**c**) AF@VMT-1, (**d**) AF@VMT-2, (**e**) AF@VMT-3, (**f**) AF@VMT-4, and (**g**) AF@VMT-5 paper. **h** Elemental mapping images of the AF@VMT-5 paper. The graph on the right shows the weight comparison of various elements in the AF paper and AF@VMT-5 paper. (**i**) Limited oxygen indices (LOI) of different types of paper. **j** Photographs of the combustion process of conventional cellulose, AF and AF@VMT-5 paper during flame-retardant tests. **k** Stress–strain curves of the AF paper and AF@VMT-x papers.

Characteristics of all-natural composite paper

Figure 2a depicts the manufacturing process of the all-natural composite paper from alginate fiber and VMT nanosheets (AF@VMT composite paper). The optical photographs of different VMT contents show that the color of the laminated paper gradually changes from white to brown as the comtent of VMT increases. The SEM images in Fig. 2b–g show a gradual increase in the number of VMT nanosheets in the composite paper. As clearly depicted in Fig. 2g, the VMT nanosheets are uniformly distributed in the fiber spaces and adhered to the alginate fibers. Figure 2h shows the energy dispersive spectrometer (EDS) mapping image of the AF@VMT-*5* paper, indicating the uniform distribution of Si, Al, Mg, and Fe elements throughout the composite paper. The main elements of alginate fiber paper (AF paper) are C, O, and Ca (Supplementary Fig. 1). In the AF@VMT-*5* paper, the mass percentages of Si, Al, Mg, and Fe elements reach 11.84%, 2.92%, 8.13%, and 1.84%, respectively, indicating the even distribution of VMT in the framework of alginate fibers. As shown in the FT-IR spectra (Supplementary Fig. 2), the characteristic peaks at 1592, 1409, and 1006 cm^{-1} are ascribed to the stretching vibration of C = N/C = C bond, C–H bond, and C = O bond, respectively. The existing hydrogen bonds in the alginate fibers further enhance the strength of the paper. In addition, the characteristic peak at ~616 cm^{-1} belongs to the Al–O bond, which only occurs in the AF@VMT sample, thus giving a good indication of VMT in the composite paper.

In addition, the VMT nanosheets confers the composite paper with an even better fire-retardant ability, as shown in Fig. 2i, j. Moreover, the AF@VMT-*5* paper has a better thermal stability than the AF paper (Supplementary Fig. 3). Because VMT has excellent fire and heat insulation properties. Alginate fiber paper (1.5 × 4 cm) had a slow negative combustion phenomenon during the burning process. As the burning time increased, the flame of alginate fiber paper gradually extinguished and burned completely within 1 min. In contrast, the traditional cellulose paper was quickly wrapped in the flame after 1 s of ignition, and it took only 4 s from the beginning of burning to all the ashes. Although the prepared AF@VMT-*5* paper had a similar phenomenon of negative combustion, the burn was basically stopped after 50 s. This is due to the extremely low thermal conductivity of VMT nanosheets, during the combustion, the VMT layer produces more coke due to the metal ions in its structure[32]. The coke produced forms a protective layer which reduces the oxygen supply, thus inhibiting the combustion reaction and extinguishing the flame, while VMT contains refractory compounds such as SiO_2, Al_2O_3, and MgO, which are responsible for the formation of inert gases from the char layer[33,34]. During the combustion process, the VMT releases H_2O, CO_2, NO, and SO_2[35], all of which are well-known fire-extinguishing agents. We compared the ultimate oxygen index of the three types of paper, and the ultimate oxygen index of the AF@VMT-*5* paper was able to reach 45%, which undoubtedly further illustrates the flame-retardant performance. In addition, we tested the mechanical properties of the composite paper. After

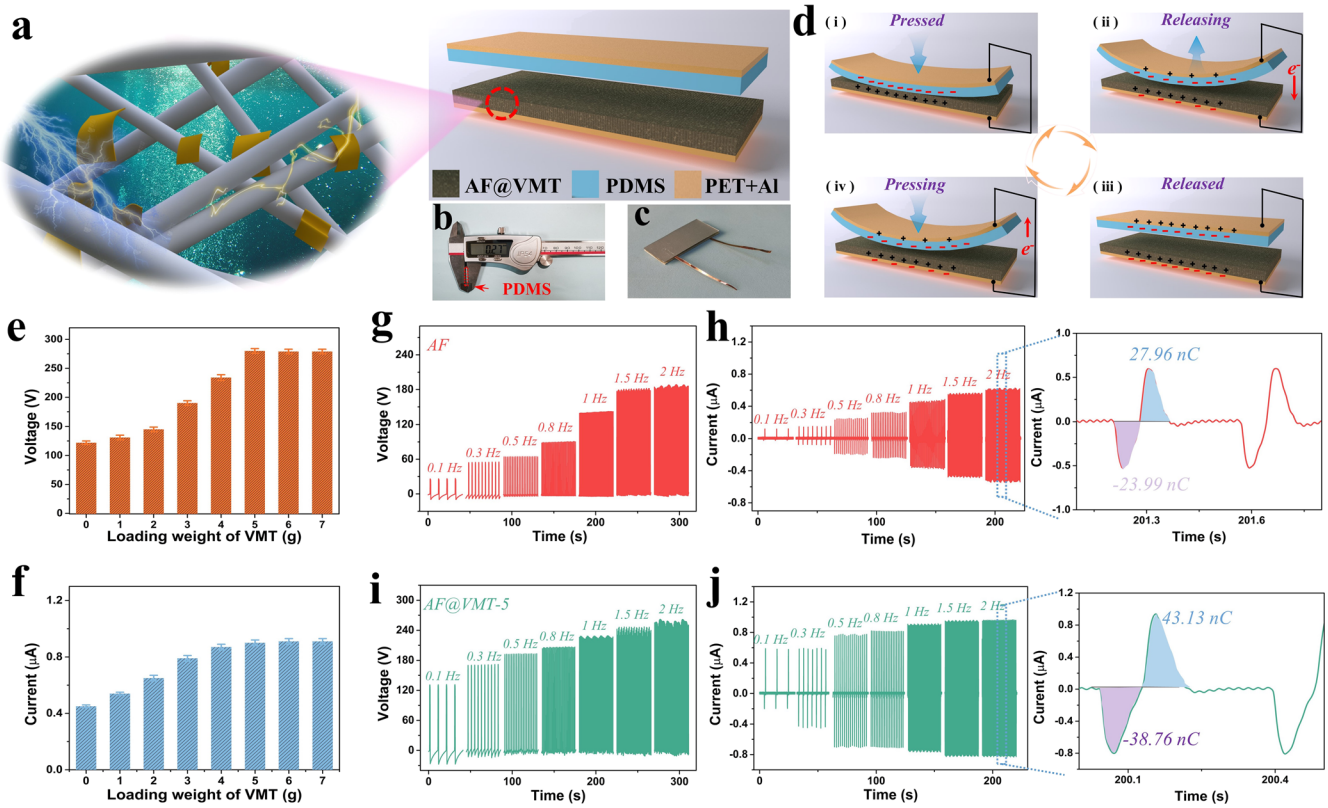

Fig. 3 Performance of triboelectric sensor. Output performance of the TENG in contact-separation mode. **a** Schematic diagram of the structure of TENG. **b**, **c** Optical photographs of the **b** PDMS friction layer and **c** final TENG device. **d** The operation mechanism of TENG and the flow of positive and negative charges. **e**, **f** Changes of output voltage and current of the TENG with different loading weight of VMT at 1 Hz frequency. **g**, **h** Output voltages and currents of AF paper TENG at different contact-separation frequencies. **i**, **j** Output open-circuit voltage and output current dependence on different contact-separation frequencies for AF@VMT-5 paper TENG.

adding 5 g VMT nanosheets, the tensile strength increases from 3.1 MP to 6.4 Mpa (Fig. 2k).

Performance of triboelectric sensor

In order to evaluate the output performance of AF@VMT composite paper as friction material, a vertical contact-separation mode triboelectric nanogenerator (CS-TENG) was constructed, since the CS-TENG becomes the most popular device mode due to its simple structural design, high instantaneous power density, and other advantages[36,37]. As schematically shown in Fig. 3a, the TENG was assembled by using PDMS film as the negative friction layer, AF@VMT composite paper as the positive friction layer and aluminum foil as both the top and bottom electrodes. As well-known, the electrical output of a TENG heavily depend on the contact area[10], shock frequency[17], and distance between frictional pairs[38], etc. Herein, the PDMS film thickness was controlled within 0.3 mm, the size of the friction layer was kept at 4 × 1.5 cm, and the separation distance between the triboelectric pairs was fixed at 2 mm, as shown in Fig. 3b, c. External forces of different frequencies were applied using linear motors. Since the device is supported by glass spacers on both sides, the real effective area of contact between the two friction layers is less than the set value (4 × 1.5 cm). In the contact-separation mode, the basic mechanism of power generation depends on the contact charging and electrostatic induction processes occurring in the frictional electric material. During the frictional contact process, the positive material tends to lose electrons and the negative material tends to attract electrons[39]. Figure 3d shows the basic working principle of the AF@VMT TENG under vertical compression force. In the pristine state, the frictional electric pairs are separated and remain electrically neutral in the absence of charge. Once the device is subjected to an external force (Fig. 3d(i)), an equal amount of opposite surface charge is transferred in the contact region between the composite paper and PDMS due to the frictional electric effect. Based on the frictional electric series, electrons from the composite paper transferred to the PDMS, resulting in a net positive charge on the composite paper surface and a net negative charge on the PDMS surface. As a result, an internal potential is generated. After the release process (Fig. 3d(ii)), the charge will flow through the load between the electrodes in order to achieve energy balance. After the release (Fig. 3d(iii)), the bottom electrode maintains the same amount of positive charge as the negative charge of the electrodes on the surface of the composite paper due to electrostatic induction. Thereafter, when the TENG is subjected to an external force again (Fig. 3d(iv)), the original electrostatic equilibrium is broken, causing the electrons from the top electrode to flow back to the bottom electrode. In the case of successive compression and release, a mixed positive and negative transient voltage is generated[7].

To investigate the effect of VMT nanosheets incorporation on the electrical output of TENG, Fig. 3e, f shows the measured output voltages and currents of the composite paper TENG under different loading weights of VMT, where the applied force frequency was kept at 1 Hz. As shown in Fig. 3e, f, the output voltage and current of the composite paper continuously increase with the addition of VMT nanosheets from 1 to 5 g. The TENG output is 120 V/0.4 μA for the AF paper while 270 V/1 μA for the AF@VMT-*5* paper. After overdosing 5 g of VMT nanosheets, the improvement of output performance is slight, and thus the optimal loading weight of VMT is defined to be 5 g. The output of the TENG is dependent on the input frequency, or

more precisely, the speed of motion. Subsequently, when the frequency dependence of the output performance of the TENG was explored, both the output voltage and current gradually increased with increasing frequency in the frequency range of 2 Hz. As compared with the AF paper-based TENG, the peak voltage/current of the AF@VMT-*5* paper-based TENG at 2 Hz frequency increased significantly from 180 V/0.5 μA (Fig. 3g, h) to 270 V/1 μA (Fig. 3i, j). By integrating the current, the amount of transferred charge also had a significant increase from 27.96 to 43.13 nC, as compared with that of pure alginate fiber paper. Herein, the improved electrical performance of the AF@VMT-*5* composite paper is attributed to the optimized composition and surface microstructure after adding VMT nanosheets. On the one hand, some trivalent Al^{3+} partially replaces the central tetravalent Si^{4+} of the tetrahedral silicate in VMT, resulting in the negatively charged nature of the VMT nanosheets. On the other hand, the VMT nanosheets enlarge the effective triboelectric area and increase the effective dielectric constant. Overall, the manufactured TENG based on composite paper and PDMS is well suited for biomechanical energy harvesting at low frequencies. The developed TENG can power various electronics by harvesting mechanical energy from the surrounding. For this purpose, the TENG can be connected to mechanical vibration sources, such as human motion, vibrating machinery, to efficiently utilize the wasted mechanical energy. Besides, the alginate fibers and VMT nanosheets are interlaced to form a complex and dense spatial network, increasing the strength of the all-natural composite paper.

Stability and charging profile of triboelectric sensor

For practical applications, the TENG must work for long periods of time, which raises the question of the durability and mechanical stability of the friction layer. Figure 4a shows the durability of the device continuously working for about 3 h (>10,000 cycles). The open-circuit voltage is almost constant throughout the test and the pulses have almost the same amplitude and peak pattern, indicating the high repeatability and durability of the AF@VMT-*5*. To investigate the stability issue, the output performance of the AF@VMT-*5* TENG was tested after one hundred days, as shown in Fig. 4b. It was found that the voltage was stable with no significant drop. As for flexibility, the output voltage of AF@VMT-*5* TENG was recorded after bending, compressing and twisting. As shown in Fig. 4c, the output electrical properties remained basically stable even if the TENG was arbitrarily deformed. With an external force applied at a frequency of 1 Hz, the resulting voltage directly lights up 70 small bulbs connected in series, as shown in the inset of Fig. 4d. To evaluate the output power of the AF@VMT-*5* TENG, resistors with various resistance values (10^3–10^{10} Ω) were connected as external loads. As shown in Fig. 4d, the power density (P) can be calculated by Eq. (1) as follows:

$$P = V^2/R_L A \quad (1)$$

where V represents the peak output voltage, R_L represents the load resistance, and A represents the TENG's effective size. Similar to the previous report[40,41], the output voltage increases with the external load resistance, where the TENG can reach a maximum output power density of 120 mW m^{-2} with a matched load of 10^8 Ω, in accordance with Ohm's law. Afterward, we rectify the signals generated by the prepared AF@VMT-*5* TENG by introducing a rectifier circuit (Fig. 4e)[42]. These rectified output signals can charge the capacitor during the pressing and releasing motion of the TENG. Figure 4e shows the capacitor charging behavior of the AF@VMT-*5* TENG, examined using different capacitor values (0.47, 4.7, and 10.0 μF). The 0.47 μF capacitor can reach 30 V in a few minutes. In addition, the charging rate of the capacitor could be simply altered by changing the striking frequency (Supplementary Fig. 5). As expected, the saturation voltage decreases with increasing capacitance value. The inset of Fig. 4e shows the enlarged view of the capacitor charging process, which portrays the voltage increase during the pressing and releasing of the capacitor by the TENG[43,44].

Potential application of triboelectric sensor

It had been reported that there is a high utilization value of the voltage signals generated from human body activities[45,46]. Based on its electrical properties, VMT fiber-based composite paper sensors can successfully monitor subtle signals and body movements, showing potential applications in rapid, real-time, non-invasive assessment of human health. Eight types of body motion were successfully monitored while biomechanical energy from the motions were simultaneously harvested, as shown in Fig. 5a–g. We fixed the device at the finger joint, which generates a real-time voltage response when the index finger is bent and straightened, and the signal strength increases as the bending angle increases (Fig. 5g). The health of joints such as the knee, elbow, and wrist are critical to human movement, especially for the elderly and athletes. We found that by fixing the device at different joints, the TENG not only provides a stable and sensitive response to continuous movement changes but also the movement of different joints generates different response signals. It is worth noting that the movement of the laryngeal junction during swallowing is not strictly an up-and-down periodic movement, so two peak responses are generated during each swallow (Fig. 5e). In addition, the signal response of the fixed device on the muscle is significantly weaker than the response at the joint (Fig. 5b), due to the degree of deformation of the muscle and the much weaker force on the device during the motion compared to the other joint motion. From these demonstrations, it is evident that we have fabricated devices that can be used to measure small movements of the human body without any external power source, while various physiological features and movement behaviors can be translated into readable, quantifiable, real-time voltage signals that facilitate parallel and whole-body physiological and movement monitoring. Therefore, it is expected that our device will have promising applications in the fields of personal health monitoring, rehabilitation of patients, athletic performance monitoring, and human motion tracing for entertainments[47–49].

Human motion prediction

To distinguish the signal responses of sensors to different joint motions in monitoring human motion, an artificial intelligence-based statistical data analysis can be adopted to exploit the regularities and differences in sensor responses that are difficult for humans to perceive from a large amount of characteristic parameter data. To capture the clustering features of the target motion, a PCA is performed using the three extracted features. PCA is an orthogonal linear transformation that maps data to a new coordinate basis via a scalar projection, which serves as a dimension reduction technique to keep the essence of the data while providing plottable axes through the first two (or three) PCs[50]. For better visualization, we reduce the multi-dimensional dataset of the extracted parameters into 2D space (PC1, PC2). Figure 6a shows the PCA scatter plots for nine different human motions. Not only can the dense arrangement of single movements of the same type be easily identified but also the clusters representing individual movements can be clearly and effectively distinguished from each other. It indicates that PCA can be an adequate solution to reduce mass data into two meaningful principal components for the machine-learning dataset. To corroborate a scheme to discriminate the different motion among the nine different groups, we employ supervised machine-learning approach by using the extracted PCs as the feature data of machine learning. The KNN is selected for classification as no assumption is required for its decision boundary. Figure 6c shows

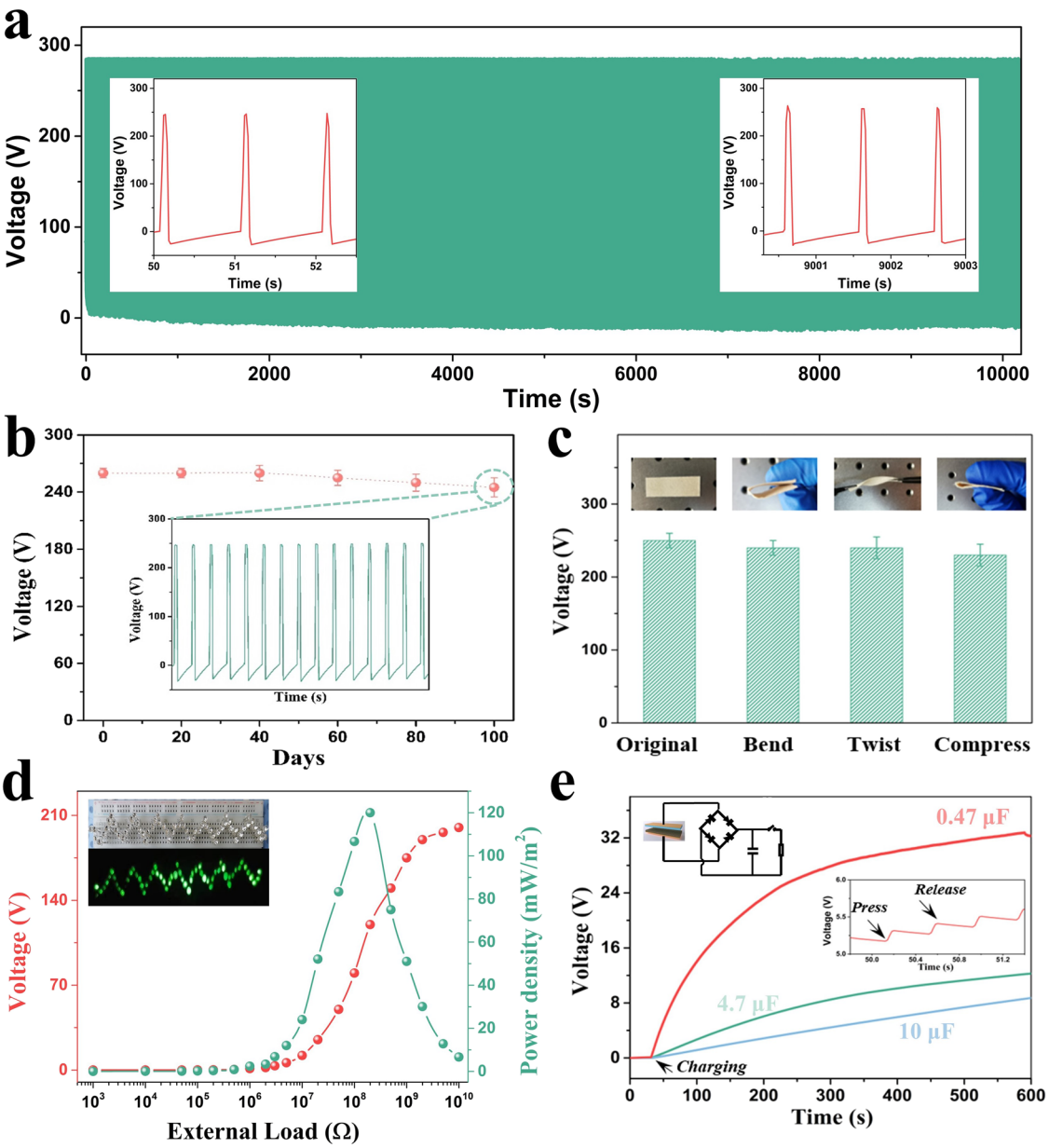

Fig. 4 Stability and charging profile of triboelectric sensor. a Endurance of AF@VMT-5 TENG over 10,000 cycles at 1 Hz. Inset shows the partial enlargement of the test around 50 s and 9000 s. **b** Long-term stability of AF@VMT-5 paper TENG, inset shows a partial enlargement of the test after 100 days. **c** Output performance of TENG before and after arbitrary deformation under repeated compressive force at 1 Hz. **d** Output power density and voltage of the AF@VMT-5 TENG with different external load resistances, about 70 small bulbs connected in series can be lit by the device, as shown in the illustration. **e** Charging profile of different capacitors by using the AF@VMT-5 TENG. Inset shows the enlarged detailed view of the capacitor charging event.

the confusion matrix for nine different types of motion from the KNN classification results ($K = 2$, Supplementary Fig. 6), showing a prediction accuracy of 96.2%. Consequently, this is able to express the decision boundary map as a function of 2D PC coordinates with excellent visibility and prediction accuracy of the training model. To build a training model for predicting the bending angle, a regression model is trained for different angles using linear regression from the Sklearn machine-learning library without data on the middle angle of the bend (about 60°). To evaluate the performance of the training model, we carefully divide the dataset into two categories for training and validation (untrained). In order to predict intermediate angles, larger and smaller angles are used only for training the model. Consequently, we are able to use the untrained dataset to verify the validity of the predicted concentration data the model has not previously seen. In addition, we further optimize the training model to return the predefined discrete prediction levels instead of a linear prediction surface consistent with the mean of a probability distribution. The predicted results of the joint flexion angle are shown in Fig. 6d. The accuracy (R^2) can be calculated using the residual scatter from the fitting line (black dashed line) by Eq. (2) as follows:

$$Accuracy\left(R^2, \%\right) = 1 - \frac{\sum(y-p)^2}{\sum(y-\overline{y})^2} \quad (2)$$

where y is the real value, p is the predicted value, and $\overline{y}$ is the average of the actual values at the corresponding joint bending angle specified, y-p can be described as a residual scatter from the prediction of the real value through the machine-learning

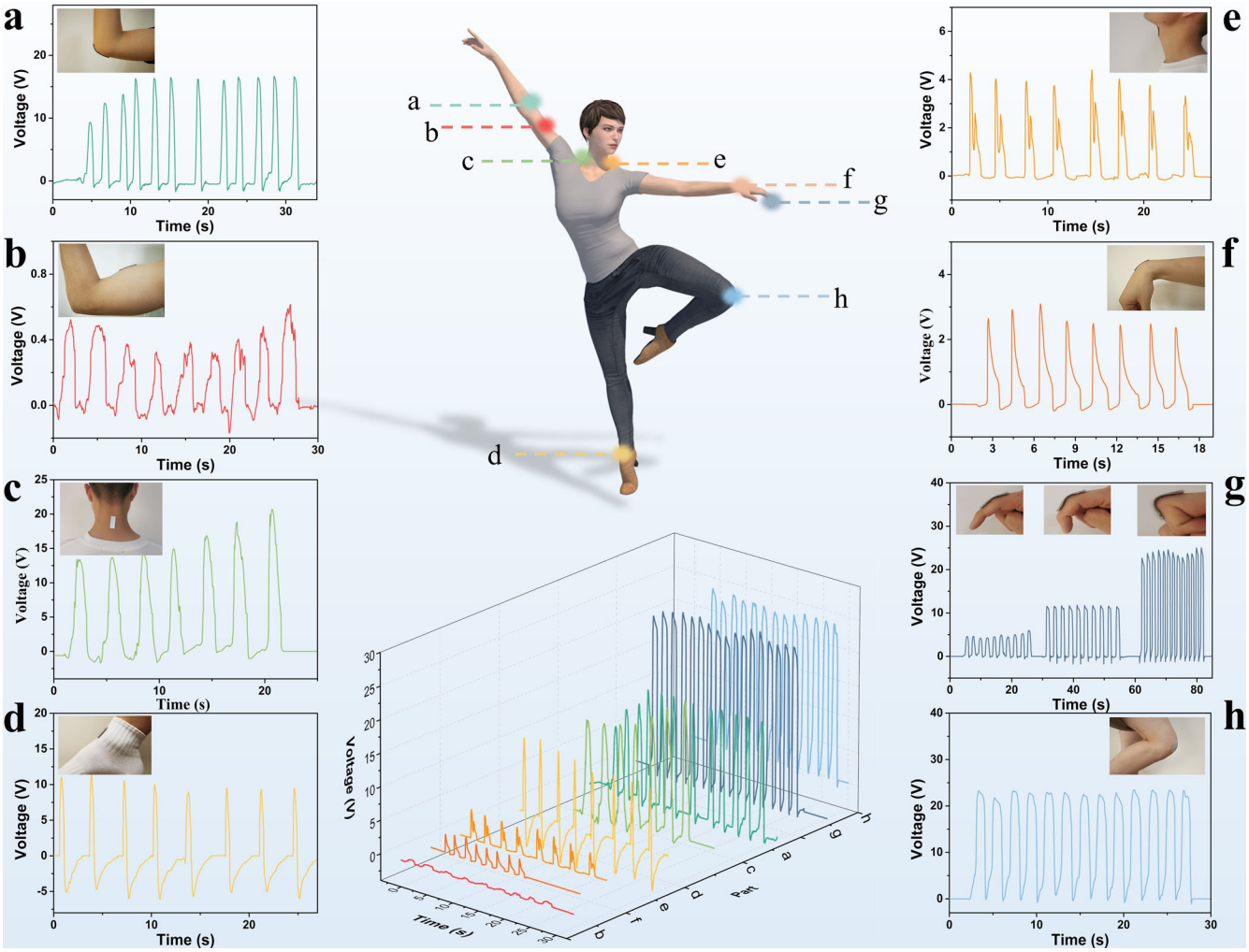

Fig. 5 Potential application of the triboelectric sensor. Real-time monitoring of human movements using AF@VMT-5 paper-based TENG. **a** Voc signals generated by elbow bending. **b** Voc signals generated by biceps firing. **c** Voc signals generated when raising and lowering the head. **d** Voc signals generated when flexing the ankle. **e** Voc signals generated by throat swallowing. **f** Voc signal generated by wrist movements. **g** Voc signals generated when the fingers are bent at different angles. **h** Voc signals generated during knee flexion movement.

results[51]. In general, the R^2 value can be used to estimate the accuracy of the training model since a higher R^2 leads to a good fit of the model compared to the true value. The results of machine learning showed 99.8% accuracy in predicting the joint bending angle. From these results, we can conclude that our PCA-based preprocessing provides significant visualization assistance for the reduced PC dimensional space through the classification of different joint movements and their angular variations, extending the available techniques for analyzing human motion through ML-based recognition.

In the current urgent need for sustainable energy solutions, all-natural phyllosilicate-polysaccharide triboelectric sensor proves to be a strong candidate for mechanical energy harvesting and self-powered sensors. The addition of VMT nanosheets gives the composite paper even better flame-retardant properties enabling its application in extreme environments and improves the output performance of marine-derived alginate fibers as the friction layer material. Due to the excellent frictional electrical properties, easy mass manufacturing, high flexibility and excellent stability, we used it for collecting useful energy and monitoring human activities in real time. The results show that signals from different joint movements of the human body are successfully collected. In addition, a machine intelligence recognition framework based on the all-natural phyllosilicate-polysaccharide triboelectric sensor were developed, which shows extraordinary accuracy in identifying different human joint movements. The classifier allows a clearly distinguishable decision boundary map with 96.2% accuracy. Moreover, the regression model was able to predict untrained joint motion at different angles with high accuracy and showed a prediction accuracy of 99.8%. Our results provide a powerful solution for re-predicting complex human joint motions. The sensor can be used for a variety of human motion detection and physiological signal monitoring, demonstrating its great potential for applications in rehabilitation training, human-machine interaction, intelligent robotics, and healthcare.

METHODS

Preparation of AF@VMT paper

First, the 20 g of vermiculite (VMT, Engineering Laboratory of Chemical Resources Utilization in South Xinjiang of Xinjiang Production and Construction Corps) granules (2–4 mm) were crushed into 70–300 mesh powder in the ultrasonic cell pulverizer (JY88-IIN, Shanghai HUXI Co., Ltd.). Firstly, a certain amount of VMT powder was added in deionized water and then sonicated in a cell crusher for 30 min to obtain VMT nanosheet solution. Then, the 3 g calcium alginate fibers (AF, Yuanhai New Material Technology Co., Ltd.) were sheared into small pieces of 1–2 mm in length and

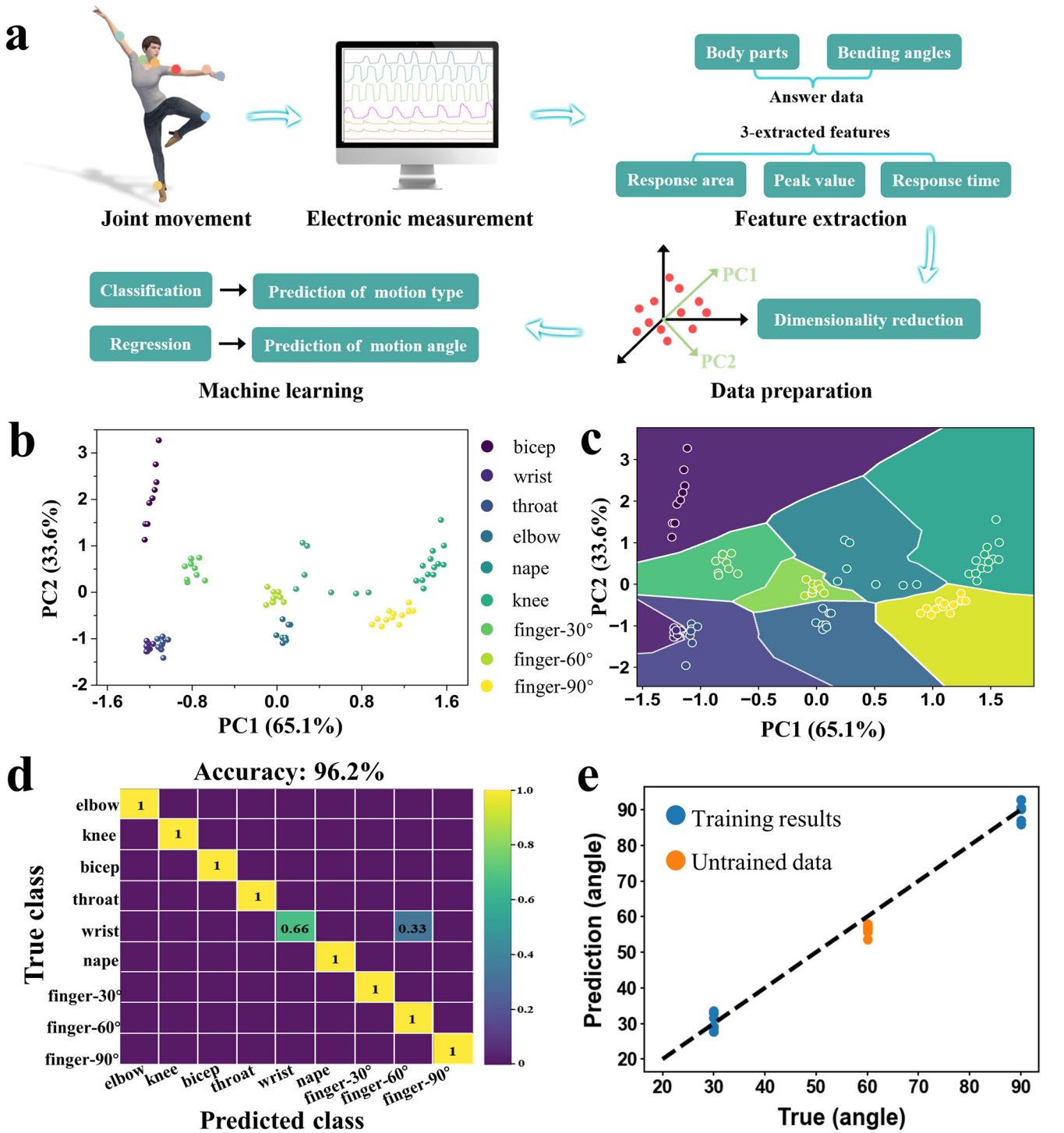

Fig. 6 Human motion prediction. **a** Schematic illustration of the data preparation for principal component analysis (PCA)-assisted classification. **b** PCA scatter plot of nine types of joint motions. **c** Decision map of nine groups classified by applying a k-nearest neighbor (KNN) of ML model with *K*-fold validation ($K = 2$). **d** Confusion matrix of nine joint motions from KNN classification results. **e** Predicted finger bending versus the actual bending angle.

soaked in appropriate amount of deionized water for 6 h. Subsequently, the above AF solution and VMT solution were mixed together in a fiber dissociator (CBJ-A, Shandong Anne Mate Instrument Co., Ltd) to disperse and dissociate at 5000 rpm. Then, the fully disintegrated pulp was poured into the paper machine (AT-CZ-2, Shandong Anne Mate Instrument Co., Ltd.) to prepare AF@VMT paper. Herein, 1, 2, 3, 4, 5, 6, and 7 g of VMT powder was applied to prepare AF@VMT paper with different VMT amount, and thus the obtained samples were denoted as AF@VMT-*x*, where "*x*" represents the weight of the added VMT.

Fabrication of triboelectric nanogenerator (TENG)

The PDMS (Dow Silicones Co., Ltd.) elastomer and the curing agent were mixed at a mass ratio of 10:1 and degassed in a vacuum oven for 30 min. After that, the transparent PDMS solution was

spin-coated onto a glass plate at 500 rpm. After that, the uncured PDMS solution after spin-coating, was put into the oven and cured at 80 °C for 40 min, and then the PDMS film was carefully removed from the glass plate. In order to have good structural support and elastic recovery, two PET films with size of 4 × 1.5 cm were used as support substrates; commercial Al foil tapes were glued on each side of the PET films. Subsequently, AF@VMT paper was glued on one of the Al foil measurements as a negative friction layer, and PDMS of the same size was glued on the other Al foil side as a positive friction layer; two insulating spacers (0.2 × 1.5 cm) were cut from the microscope slide for separating the friction layers with a spacing of 2 mm. After that, two copper wires were connected to the electrodes to facilitate device connection to the measurement instrument. The tapes used for the experiments were all commercial 3 M tapes. Finally, the vibration sensor device was encapsulated with the help of transparent adhesive tape.

Characterization and measurement

The morphology of the samples was observed using a scanning electron microscopy (SEM, Quanta 250 FEG) and a transmission electron microscopy (TEM, JEM 2100 F). The exfoliated VMT solution was spin-coated onto the silicon substrate and the thickness of the nanosheets was measured by an atomic force microscope (AFM, Keysight 5500). The functional groups of the samples were characterized by Fourier transform infrared spectroscopy (FT-IR, Nicolet iS10). The zeta potential of the VMT solution was measured with Nano ZSE and the results are expressed as the average of three measurements. A thermogravimetric analyzer (TG 209 F3) was used to study the thermal stability. A certain mass of fiber paper was placed in a crucible and ramped up from room temperature to 900 °C at a rate of 10 °C min^{-1} and the mass-temperature curve of the sample was recorded. Oxygen index measuring instrument (CX-Y36) used for oxygen index measurement of fiber paper. The electrical performance testing of the TENG was characterized using a linear motor (LINMOT) applying periodic horizontal thrusts at different frequencies. The output electrical performances, such as open-circuit voltage and short-circuit current, of the TENG were measured utilizing a source measurement unit (2612B, Keithley) and a sourcemeter (6514, Keithley) controlled by a computer.

DATA AVAILABILITY

The data that support the findings of this study are available from the corresponding author upon reasonable request.

Received: 20 November 2022; Accepted: 4 April 2023;
Published online: 17 April 2023

REFERENCES

1. Wang, Z. L. Triboelectric nanogenerator (TENG)-sparking an energy and sensor revolution. *Adv. Energy Mater.* **10**, 20000137 (2020).
2. Wang, Z. et al. Stretchable unsymmetrical piezoelectric $BaTiO_3$ composite hydrogel for triboelectric nanogenerators and multimodal sensors. *ACS Nano* **16**, 1661–1670 (2022).
3. Du, X. et al. Recent progress in fibrous high-entropy energy harvesting devices for wearable applications. *Nano Energy* **101**, 107600 (2022).
4. Zhang, K. et al. Structure design and performance of hybridized nanogenerators. *Adv. Funct. Mater.* **29**, 1806435 (2018).
5. Yuan, Z. et al. Spherical triboelectric nanogenerator with dense point contacts for harvesting multidirectional water wave and vibration energy. *ACS Energy Lett.* **6**, 2809–2816 (2021).
6. Gao, G. et al. Bioinspired self-healing human-machine interactive touch pad with pressure-sensitive adhesiveness on targeted substrates. *Adv. Mater.* **32**, 2004290 (2020).
7. Doganay, D. et al. Fabric based wearable triboelectric nanogenerators for human machine interface. *Nano Energy* **89**, 106412 (2021).
8. Dong, Y. et al. Metallic MXenes: a new family of materials for flexible triboelectric nanogenerators. *Nano Energy* **44**, 103–110 (2018).
9. Peng, X. et al. A breathable, biodegradable, antibacterial, and self-powered electronic skin based on all-nanofiber triboelectric nanogenerators. *Sci. Adv.* **6**, 9624 (2020).
10. Yang, T. et al. Hierarchically microstructure-bioinspired flexible piezoresistive bioelectronics. *ACS Nano* **15**, 11555–11563 (2021).
11. Kim, D. W. et al. Material aspects of triboelectric energy generation and sensors. *NPG Asia Mater.* **12**, 1–17 (2020).
12. Khandelwal, G. et al. Materials beyond conventional triboelectric series for fabrication and applications of triboelectric nanogenerators. *Adv. Energy Mater.* **11**, 2101170 (2021).
13. Zhang, B. et al. Understanding the percolation effect in triboelectric nanogenerator with conductive intermediate layer. *Research* **4**, 7189376 (2021).
14. Yu, A. et al. Progress in triboelectric materials: toward high performance and widespread applications. *Adv. Funct. Mater.* **29**, 1900098 (2019).
15. Chen, A. et al. Polymer materials for high-performance triboelectric nanogenerators. *Adv. Sci.* **7**, 2000186 (2020).
16. Zhang, B. et al. Sustainable tunnel lighting system based on mechanical-regulated and soft-contact hybridized nanogenerator. *Nano Energy* **104**, 107868 (2022).
17. Wu, S. et al. Fabrication of polyethyleneimine-paper composites with improved tribopositivity for triboelectric nanogenerators. *Nano Energy* **93**, 106859 (2022).
18. Oh, H. et al. Highly conductive ferroelectric cellulose composite papers for efficient triboelectric nanogenerators. *Adv. Funct. Mater.* **29**, 1904066 (2019).
19. Liu, K. et al. Zinc-catecholete frameworks biomimetically grown on marine polysaccharide microfibers for soft electronic platform. *Nano Res.* **16**, 1296–1303 (2022).
20. Lin, Z. et al. Rationally designed rotation triboelectric nanogenerators with much extended lifetime and durability. *Nano Energy* **68**, 104378 (2020).
21. Wang, P. et al. Interface engineering of calligraphic ink mediated conformal polymer fibers for advanced flexible supercapacitors. *J. Mater. Chem. A* **10**, 15776–15784 (2022).
22. Zhang, M. et al. Porous oxide-functionalized seaweed fabric as a flexible breath sensor for noninvasive nephropathy diagnosis. *ACS Sens.* **7**, 2634–2644 (2022).
23. Kim, S. et al. Transparent flexible graphene triboelectric nanogenerators. *Adv. Mater.* **26**, 3918–3925 (2014).
24. Zhang, B. et al. All-in-one 3D acceleration sensor based on coded liquid–metal triboelectric nanogenerator for vehicle restraint system. *Mater. Today* **43**, 37–44 (2020).
25. Jiang, C. et al. All-electrospun flexible triboelectric nanogenerator based on metallic MXene nanosheets. *Nano Energy* **59**, 268–276 (2019).
26. Wu, C. et al. Enhanced triboelectric nanogenerators based on MoS_2 monolayer nanocomposites acting as electron-acceptor layers. *ACS Nano* **11**, 8356–8363 (2017).
27. Bhavya, A. S. et al. Massive enhancement in power output of BoPET-paper triboelectric nanogenerator using 2D-hexagonal boron nitride nanosheets. *Nano Energy* **90**, 106628 (2021).
28. Tian, W. et al. Self-assembly of vermiculite-polymer composite films with improved mechanical and gas barrier properties. *Appl. Clay Sci.* **180**, 105198 (2019).
29. Shao, J. et al. Self-assembled two-dimensional nanofluidic proton channels with high thermal stability. *Nat. Commun.* **6**, 1–7 (2015).
30. Saha, K. et al. Applications of lamellar membranes reconstructed from clay mineral-based nanosheets: a review. *ACS Appl. Nano Mater.* **5**, 15972–15999 (2022).
31. Cao, L. et al. Flexible, transparent ion-conducting membranes from two-dimensional nanoclays of intrinsic conductivity. *J. Mater. Chem. A* **7**, 25657–25664 (2019).
32. Sethurajaperumal, A. et al. A thermally insulating vermiculite nanosheet–epoxy nanocomposite paint as a fire-resistant wood coating. *Nanoscale Adv.* **3**, 4235–4243 (2021).
33. Wang, X. et al. Comparative study of the synergistic effect of binary and ternary LDH with intumescent flame retardant on the properties of polypropylene composites. *RSC Adv.* **5**, 78979–78985 (2015).
34. Wang, P. et al. Dual fire retardant action: the combined gas and condensed phase effects of azo-modified NiZnAl layered double hydroxide on intumescent polypropylene. *Ind. Eng. Chem. Res.* **56**, 920–932 (2017).
35. Zhang, W. et al. Study of the synergistic effect of silicon and phosphorus on the blowing-out effect of epoxy resin composites. *Polym. Degrad. Stabil.* **9**, 1041–1048 (2012).
36. Varghese, H. et al. A high-performance flexible triboelectric nanogenerator based on cellulose acetate nanofibers and micropatterned PDMS films as mechanical energy harvester and self-powered vibrational sensor. *Nano Energy* **98**, 107339 (2022).

37. Graham, S. A. et al. Biocompatible electrospun fibers-based triboelectric nanogenerators for energy harvesting and healthcare monitoring. *Nano Energy* **100**, 107455 (2022).
38. Park, D. et al. Biocompatible and mechanically-reinforced tribopositive nanofiber mat for wearable and antifungal human kinetic-energy harvester based on wood-derived natural product. *Nano Energy* **96**, 107091 (2022).
39. Kim, H. J. et al. Silk nanofiber-networked bio-triboelectric generator: silk bio-TEG. *Adv. Energy Mater.* **6**, 1502329 (2016).
40. Rahman, M. T. et al. Metal-organic framework-derived nanoporous carbon incorporated nanofibers for high-performance triboelectric nanogenerators and self-powered sensors. *Nano Energy* **94**, 106921 (2022).
41. Saqib, Q. et al. Natural seagrass tribopositive material based spray coatable triboelectric nanogenerator. *Nano Energy* **89**, 106458 (2021).
42. Xu, F. et al. Scalable fabrication of stretchable and washable textile triboelectric nanogenerators as constant power sources for wearable electronics. *Nano Energy* **88**, 106247 (2021).
43. Tanguy, N. et al. Natural lignocellulosic nanofibrils as tribonegative materials for self-powered wireless electronics. *Nano Energy* **98**, 107337 (2022).
44. Yang, M. et al. Green and recyclable cellulose based TENG for sustainable energy and human-machine interactive system. *Chem. Eng. J.* **442**, 136150 (2022).
45. Zhu, G. et al. Self-powered and multi-mode flexible sensing film with patterned conductive network for wireless monitoring in healthcare. *Nano Energy* **98**, 107327 (2022).
46. Luo, X. et al. A flexible multifunctional triboelectric nanogenerator based on MXene/PVA hydrogel. *Adv. Funct. Mater.* **31**, 516–523 (2021).
47. Zhang, S. et al. On-skin ultrathin and stretchable multifunctional sensor for smart healthcare wearables. *NPJ Flex. Electron.* **6**, 1–12 (2022).
48. Durukan, M. B. et al. Multifunctional and physically transient supercapacitors, triboelectric nanogenerators, and capacitive sensors. *Adv. Funct. Mater.* **32**, 2106066 (2021).
49. Yun, S. et al. Mechanically robust triboelectric nanogenerator with a shear thickening fluid for impact monitoring. *J. Mater. Chem. A* **10**, 10383–10390 (2022).
50. Jiang, M. et al. Predicting output performance of triboelectric nanogenerators using deep learning model. *Nano Energy* **93**, 106830 (2022).
51. Ogbeide, O. et al. Inkjet-printed rGO/binary metal oxide sensor for predictive gas sensing in a mixed environment. *Adv. Funct. Mater.* **32**, 213348 (2022).

ACKNOWLEDGEMENTS

This work was supported by the National Natural Science Foundation of China (Nos. 21761029, 51973099), Taishan Scholar Program of Shandong Province (No. tsqn201812055), Central Government Guiding Funds for Local Science and Technology Development (Nos. Z135050009017 and 2022ZY015), Corps Science and Technology Program (No. 2020CB019), Innovation Group Project of Tarim University (Nos. TDZKCQ201901), Xinjiang Corps famous teachers, the State Key Laboratory of Bio-Fibers and Eco-Textiles (Qingdao University) (Nos. ZKT04, GZRC202007), and the Engineering Laboratory of Chemical Resources Utilization in South Xinjiang of Xinjiang Production and Construction Corps (No. CRUZD2003).

AUTHOR CONTRIBUTIONS

K.Z., S.Y., and W.T. conceived the research. K.Z. supervised the research. Y.L. and X.Z. performed experiments and wrote the paper. W.D. conducted the machine learning. Y.S. and B.H. helped with characterization and data analysis. S.Y. guided with the human motion detection. All authors discussed the results and commented on the manuscript at all stages.

COMPETING INTERESTS

The authors declare no competing interests.

ADDITIONAL INFORMATION

Supplementary information The online version contains supplementary material available at https://doi.org/10.1038/s41528-023-00254-3.

Correspondence and requests for materials should be addressed to Weiliang Tian, Song Yang or Kewei Zhang.

Reprints and permission information is available at http://www.nature.com/reprints

Publisher's note Springer Nature remains neutral with regard to jurisdictional claims in published maps and institutional affiliations.